Mechanical Systems and Signal Processing 177 (2022) 109233

Contents lists available at ScienceDirect

Mechanical Systems and Signal Processing

journal homepage: www.elsevier.com/locate/ymssp

Streamlined particle filtering of phase-based magnified videos for quantified operational deflection shapes

Nicholas A. Valente [a], Aral Sarrafi [a], Zhu Mao [a,b,*], Christopher Niezrecki [a]

[a] Department of Mechanical Engineering, University of Massachusetts Lowell, Lowell, MA 01854, USA
[b] Department of Mechanical and Materials Engineering, Worcester Polytechnic Institute, Worcester, MA 01609, USA

ARTICLE INFO

Communicated by Janko Slavič

Keywords:
Phase-based video processing
Computer vision
Particle filter
Data clustering
Unsupervised learning
Structural dynamics identification
Total variation denoising

ABSTRACT

Non-contact optical measurements are commonly used in industrial and research domains to obtain displacement measurements. This can be attributed to their noninvasive advantages over traditional instrumentation approaches. Phase-based motion estimation (PME) and magnification (PMM) are targetless methods that have been utilized recently to extract qualitative data from structures via experimental modal analysis (EMA) and operational modal analysis (OMA). Transforming the motion-magnified sequence of images into quantified operating deflection shape (ODS) vectors is currently being conducted via edge detection. Although effective, these methods require human supervision and interference; such that, accurate characteristics of the structure are guaranteed. Within this study, a new hybrid computer vision approach is introduced to extract the quantified ODS vectors from motion-magnified images with minimal human supervision. The particle filter (PF) point tracking method is utilized to track the desired feature points in the motion-magnified sequence of images. Moreover, the k-means clustering method is employed as an unsupervised learning approach to perform the segmentation of the particles and assign them to specific feature points in the motion-magnified sequence of images. Total variation denoising is used to smooth the motion-magnified artifacts, which improves ODS vector extraction and provides a robust outlier removal. The results show that the cluster centers can be applied to estimate the ODS vectors, and the performance of the proposed methodology is evaluated experimentally on a lab-scale cantilever beam.

1. Introduction

Parameter extraction in structural dynamics applications are essential in identifying dynamic behavior induced by external excitation [1]. The applications of structural dynamics identification encompass a variety of interconnected topics such as: modal analysis, structural model validation, structural health monitoring (SHM), and production certification procedures [2,3]. Within a variety of fields such as aerospace [4,5], mechanical engineering [6-9], and civil engineering [10-15], structural dynamics identification procedure is used to better understand dynamic behavior under an external excitation. Two fundamental techniques, namely EMA and OMA have been developed and well established in the research community throughout past decades [16]. Commercial software and hardware packages are available to perform high fidelity EMA or OMA for a variety of applications. EMA utilizes both the input and output data to characterize the dynamics of the structure, while in OMA, the excitation forces are unknown and the

* Corresponding author at: Department of Mechanical and Materials Engineering, Worcester Polytechnic Institute, Worcester, MA 01609, USA.
E-mail address: zmao2@wpi.edu (Z. Mao).

https://doi.org/10.1016/j.ymssp.2022.109233
Received 10 December 2021; Received in revised form 16 March 2022; Accepted 23 April 2022
Available online 5 May 2022

Nomenclature

Symbol	
ϕ	Complex phase map
$\widetilde{\phi}$	Band-pass filtered complex phase map
α	Magnification factor
$\mathbf{X}$	Particle state matrix
$\mathbf{W}$	Zero-mean Gaussian white noise matrix
$\mathbf{A}$	State transition matrix
ζ	Distance vector relating the actual and target Red Green Blue (RGB) vector
Π	Set of dynamic states
$\overline{\Pi}$	Predicted set of a dynamic states
σ^2	Variance associated with the RGB vector
$\mathbf{Y}$	Measurement of predicted particle states
ξ	Likelihood function between the predicted and current particle state matrices
$\widehat{P}$	Location of all particles at a particular instance in time
μ	Center of point cloud cluster
$\boldsymbol{K}$	Phase-based magnified images
$\widetilde{\boldsymbol{K}}$	Smoothed phase-based magnified images
β	Regularization parameter
J	Processed images

identification is conducted based on only the output response of the structure [1]. Traditional EMA and OMA approaches require many sensors attached to the structure for larger test subjects. With this in mind, low sensing resolution due to a lack of sensors may lead to visual misrepresentation of true motion or even spatial aliasing [17]. Conversely, installing more sensors is not always feasible due to a limited number of available channels in the data acquisition system, data transmission bandwidth, and wiring accessibility to the structures [18]. In addition to this, mounted sensors may impose a mass loading effect to the testing structures [19], which distorts the extracted dynamics and may lead to false engineering decision-making. Alternative measures are currently being investigated to limit the disadvantages of typical contact sensors such as accelerometers [20].

Non-contact vibration measurements have attracted substantial attention over the past few years. Most non-contact measurement techniques typically rely on either electromagnetic radiation or more recently infrared imaging [21]. Camera-based measurements are becoming increasingly popular in the field of modal analysis and damage detection due to the accesability of computer vision algorithms and hardware technology [22-27]. Camera-based measurements are relatively low-cost, easy to implement, and provide measurements with very high spatial resolution [28,29]. Moreover, among all the image/video processing techniques, 3D digital image correlation (3D DIC) and 3D point tracking (3DPT) are widely accepted in both industrial and research applications [30-35].

The idea of phase-based motion estimation led to a new technique in computer vision and computational photogrammetry known as phase-based motion magnification. This approach was developed by Wadhwa et al. to amplify subtle movements in videos [36-39]. This ultimately results in the human vision system perceiving amplified or exaggerated motions. The first applications of PMM for structural dynamics identification was presented by Chen et al. [21,40]. Yang et al. combined both PME, PMM and the blind source separation algorithm to extract modal parameters from a vibrating structure [28]. More recently, Valente et al. determined how much motion is associated with magnification factor; such that, the use of PMM can be extended to a quantitative measurement tool [41].

The state-of-the-art method in transforming motion magnified videos into quantified ODS vectors is the Canny edge detector [21,28,42,43]. However, using Canny edge detection to extract the quantified ODS vectors requires a relatively high level of human supervision and intervention based on the reports by Chen's, Yang's, and other research papers [21,28,44]. The human supervision required by this method may be time-consuming and unreliable in some cases. Most recently, Bhowmick et al. have adopted advanced forms of optical flow and compressed sensing techniques to simplify subtle motion extraction from edge features [45,46]. Therefore, an accurate and more automated identification process needs to be investigated.

This work proposes a new hybrid computer vision algorithm to process motion-magnified videos in a semi-automatic fashion. The proposed methodology dives deeper into the concept of transforming motion-magnified videos into ODS vectors by utilizing a variety of several tools including particle filters, point tracking, and clustering. A lab-scale cantilever beam is used as a test structure for evaluating the performance of the proposed method. The motion-magnified videos are obtained by applying the PMM algorithm in several frequency bands corresponding to the resonant frequencies of the cantilever beam following. The significant contribution of the paper is in the transformation of motion-magnified videos from visual perceptions of the ODSs into quantified and well-defined ODS vectors in a semi-automatic manner. The particle filter point tracking method is used to track the feature points in the motion-magnified videos. In addition, the k-means clustering algorithm (an autonomous unsupervised statistical learning method), is applied to perform the segmentation of the particles that are tracking the feature points.

The paper starts with a brief sketch of the theoretical background on the topics that are critical to the unified computer vision approach: namely, phase-based motion estimation, phase-based motion magnification, particle filters, and k-means clustering. In

section 3, all the pieces of the methodology are put together to describe the overall workflow. The evaluation of the methodology is performed on a lab-scale cantilever beam, and the details of the experimental test setup are presented in Section 4. The results and comprehensive discussion on the outcome of the proposed approach can be found in Section 5. In the last section of the article, the conclusions are presented, which contain practical considerations of the technique as well as suggestions for future work.

2. Theoretical background

The proposed unified computer vision framework is a combination of several computer vision methodologies including: PME, PMM, particle filters, and k-means clustering. In this section of the paper, an overview of the theoretical background for each of the methods is presented, and the role of each technique is described in the final approach.

2.1. Phase-Based motion estimation

Phase-based motion estimation decomposes images into a complex valued map using a Gabor wavelet. The change of phase between two consecutive frames in video has been shown to be proportional to the motion observed between the two images. Moreover, Fleet and Jepson reported that the phase-based motion estimation often provides higher a signal-to-noise ratio (SNR) compared to other gradient-based optical flow methods. Therefore, phase-based motion estimation is more robust to contamination and variations of lighting conditions [47]. The subtle motion that is seen in video can be difficult to extract; therefore, current state-of-the art methodologies rely heavily on changes in pixel intestines. Rather than relying on pixel based approaches, this paper will aim to estimate the subtle motion between images by utilizing the change in image phase over a given period of time. $I(x,y,t_n)$ is considered the intensity of the pixel at a specific location (x,y) at time, t_n. In the sequential frame, a motion vector $(\Delta x, \Delta y)$ is applied on the previous image $I(x,y,t_n)$, which is represented as $I(x+\Delta x, y+\Delta y, t_{n+1})$. The brightness consistency assumption states that illumination of the object is consistent at times t_n and t_{n+1}. Therefore, it can be shown that intensities are independent of time or

$$I(x+\Delta x, y+\Delta y, t_{n+1}) = I(x+\Delta x, y+\Delta y, t_n). \tag{1}$$

A Gabor wavelet will be used to decompose images into a complex valued map [48], which is defined as [49]:

$$g(x,y,\lambda,\theta,\psi,\sigma,\gamma) = e^{\left(-\frac{x'^2+\gamma^2 y'^2}{2\sigma^2}\right)} e^{i\left(2\pi\frac{x'}{\lambda}+\psi\right)}. \tag{2}$$

The orientation of the Gabor wavelet and its respective coordinates, (x', y'), are described by the parameter θ below:

$$\begin{aligned} x' &= -x\cos\theta + y\sin\theta, \\ y' &= x\sin\theta + y\cos\theta. \end{aligned} \tag{3}$$

The orientation of the Gabor wavelet in Equation (3) indicates its sensitivity to the motion in that specific direction. For example, for $\theta = 0^o$, motion in x-direction will be captured. Likewise, for $\theta = 90^o$, motion in y-direction will be captured. The other parameters in the Gabor wavelet definition $(\lambda,\psi,\sigma,\gamma)$ are not relevant to the motion estimation process, and details of those parameters are presented in [44,48]. The complex Gabor wavelet can be represented as the summation of its real and imaginary parts as below:

$$g(x,y,\lambda,\theta,\psi,\sigma,\gamma) = G_\theta + iH_\theta. \tag{4}$$

The first stage of PME is to decompose each of the frames captured in video into the complex domain using the following transformation:

$$C(u,v,t_n) = \int_{-\infty}^{+\infty}\int_{-\infty}^{+\infty} I(x,y,t_n) g(x-u, y-v; \lambda,\theta,\psi,\sigma,\gamma)\,dxdy. \tag{5}$$

Considering that $C(u,v,t_n)$ is a complex number, $C(u,v,t_n)$ can be expressed more concisely in polar form:

$$C(u,v,t_n) = A(u,v,t_n)e^{i\phi(u,v,t_n)} \tag{6}$$

Moreover, it can be shown that the difference between the phase values in two consecutive frames is proportional to true motion [44]:

$$\begin{aligned} &\Delta x \propto \phi(u,v,t_{n+1}) - \phi(u,v,t_n) \quad \text{if} \quad \theta = 0 \\ &\Delta y \propto \phi(u,v,t_{n+1}) - \phi(u,v,t_n) \quad \text{if} \quad \theta = \frac{\pi}{2} \end{aligned} \tag{7}$$

The detailed derivation of the algorithm can be found in [44]. Equation (7) indicates that the motion is proportional to the change in phase. However, phase is bounded on the interval length of 2π, due to phase being a cyclic variable. Therefore, the relative motion between the two frames cannot exceed 2π because the large phase variations will introduce motion estimation errors or spatial aliasing, which can affect accurate quantification. In vibration applications the relative motion between two consecutive frames is typically small; therefore, the extraction of phase from sequential frames would not typically exceed 2π unless a large amount of motion amplification takes place. For this application, the extraction of phase values from successive images permits the estimation of a motion time series.

PME is used as the first step of structural dynamics identification and the sequence of images are then processed. As previously discussed, phase variation is proportional to the motion to be estimated. As a result, the frequency content of the extracted phase variation should be nearly identical to the real motion. Therefore, resonant frequencies of the structure will be extracted in the frequency domain. This is achieved by analyzing the frequency content of the extracted phase variation time-series.

2.2. Phase-based motion magnification

PME can estimate the motion associated with the pixels corresponding to the dynamics of the test structure. PMM is an extension to PME that can reconstruct a new video with amplified motions within preselected specific frequency bands. It has been shown that magnifying the motions in a narrow frequency band for a video captured from a vibrating structure is able to generate a video that represents the ODS of the structure associated with that specific frequency [36,50].

Within this section, the PMM approach will be described, and the detailed derivations and discussions are available in [36,38,41]. As discussed in the theoretical background of PME, the phase variation in Equation (6) is proportional to true motion. Temporal-filtering and amplifying phase variations in Equation (6), allows the modified phase-variations to produce magnified motions in the selected frequency band. If the series of complex-valued phase maps and its respective coordinates (u, v) from the original video ranging from frame $(0 : n)$ are represented as $\phi = (u, v, t_{0:n})$ and $A(u, v, t_{0:n})$, the phase series $\phi = (u, v, t_{0:n})$ can be filtered by a band-pass filter. Applying the filter, **F**, along the time dimension leads to a new series of phase maps,$\widetilde{\phi} = (u, v, t_{0:n})$. Equation (8) represents the band-passed sequence of phase maps.

$$\widetilde{\phi} = (u, v, t_{0:n}) = \boldsymbol{F}[\phi(u, v, t_{0:n})] \tag{8}$$

In Equation (8), **F** is a linear band-pass filter in the time domain. After applying the band-pass filter on the phase variations, a new set of magnified images can be mathematically obtained as:

$$\overline{I}(x, y, t_{0:n}) = A(u, v, t_{0:n}) e^{i\left(\widetilde{\phi}(u, v, t_0) + (1+\alpha)\widetilde{\phi}(u, v, t_{0:n})\right)} \tag{9}$$

Equation (9) expresses the motion magnified images, which contain the same amplitudes $A(u, v, t_{0:n})$ with a magnified phase sequence $\widetilde{\phi}(u, v, t_0) + (1+\alpha)\widetilde{\phi}(u, v, t_{0:n})$. The subtle motion in the phase series is being magnified by a magnification factor α with respect to the reference phase $\widetilde{\phi}(u, v, t_0)$. A selection of the band-pass filter's center frequency, f_c and tuning the width of the passband, b will result in a magnified video that reflects the ODS of the structure. As demonstrated by Valente et al., α should be determined selectively rather than arbitrarily to limit the presence of spatial aliasing and ensure accurate quantification [41].

2.3. Particle filter

The particle filter is considered one of the most powerful and widely used tools in the context of state estimation techniques [51], due to its significant flexibility compared to the Kalman filter. The Kalman filter is the optimal solution when both process and measurement noise are Gaussian distributed and system dynamics are linear [52]. However, a particle filter can better handle noise containing an arbitrary distribution and non-linear system dynamics [53,54]. It should be noted that, for non-linear systems, extensions of the Kalman filter such as the Extended Kalman Filter (EKF) or the Unscented Kalman Filter (UKF) have been designed. In addition, the Kalman filter is classified as a unimodal estimator where typically only one feature or object can be tracked over a series of time. In contrast, a particle filter can provide multimodal estimations, where multiple objects in a scene can be tracked which permit further analysis of complex dynamics [55,56]. For tracking multiple targets in the sequence of images, particle filters are more feasible and promising. The particle filter algorithm is suitable for high dimensional state-spaces, such as tracking problems in videos. Its performance can outplay the other category of multimodal estimation methods such as the histogram filter, which is computationally intensive in high-dimensional state spaces [57].

In this section, a sketch of the particle filter algorithm for state estimation is provided, and the practical considerations for solving the tracking problem using particle filters are discussed. The states of the system in the tracking problem are going to be assumed as the location and velocity of the desired target on the *x*-*y* plane as:

$$\mathbf{X}_i = [x_i, y_i, c_i, d_i]^T. \tag{10}$$

In Equation (10), $(c_i, d_i) = (\dot{x}, \dot{y})$ or the velocities of the target in the *x*-*y* plane. The dynamics of the system are going to be assumed as a constant velocity model for all particles. The constant velocity linear model can be expressed as follows:

$$\mathbf{X}_i = \mathbf{A}\mathbf{X}_{i-1} + \mathbf{W}_i \tag{11}$$

where **A** is the state transition matrix and $\mathbf{W_i}$ is a zero-mean Gaussian white noise matrix. The state transition matrix for the constant velocity model is:

$$\mathbf{A} = \begin{bmatrix} 1 & 0 & \Delta t & 0 \\ 0 & 1 & 0 & \Delta t \\ 0 & 0 & 1 & 0 \\ 0 & 0 & 0 & 1 \end{bmatrix} \tag{12}$$

The time-step integration size for this application is set to $\Delta t = 1$ (s). The robustness nature of the particle filter is able to correct and adjust the state transition model to what is being overserved throughout the video. This adjustability will prove to be important when estimating the motion of higher order vibrations. $\mathbf{Y}_i$ are considered the Red Green Blue (RBG) intensities of the pixels. At this point, the system model, the states of the state-space matrix, and the observable states are defined for the particle filter-tracking problem. The missing piece relating these components is the likelihood function associated with a specific particle. In this work, the measurement likelihood function is evaluated based on the Euclidian distance between the observed RGB value of a pixel, denoted as $\overrightarrow{RGB_p}$, and a target RGB vector denoted as $\overrightarrow{RGB_t}$. As a result, the likelihood function for m states can be expressed as:

$$P\left(\mathbf{Y}_i \middle| \mathbf{X}_i^m\right) = \frac{1}{\sqrt{2\pi\sigma}} e^{\left(-\frac{\zeta^2}{2\sigma^2}\right)}, \tag{13}$$

where ζ in Equation (13) is the distance between $\overrightarrow{RGB_p}$ and $\overrightarrow{RGB_t}$ as defined in the following equation:

$$\zeta = \|\overrightarrow{RGB_t} - \overrightarrow{RGB_p}\|_2. \tag{14}$$

Particles are samples of a posterior distribution of unknown quantity concerning the states $\mathbf{X}_i$ [57]. In this problem, each particle is a vector consisting of four elements $\mathbf{X}_i^{index} = [x_i, y_i, c_i, d_i]^T$. $\mathbf{X}_i^{index}$ is a sample of the posterior distribution of states at time step i. The statement of the particle filter algorithm outlined in Fig. 1.

The particle filter algorithm, as described in the workflow above, does not state any limitations regarding the type of noise distribution or nonlinearity. Also, it should be noted that the estimation is multimodal, and all the likely estimations will be captured with the particle filter algorithm. These are among the main advantages of the particle filter over the Kalman filter for structural dynamics analysis.

The performance of the particle filter tracker will be investigated on a sample video. Fig. 2(a) where the objective is to track the red disk as the target through its trajectory. This sample video was synthetically generated and captured at 10 (fps).

The parameters that are defined by the user are $\overrightarrow{RGB_t}$ and the variance, σ^2 associated with said vector. The user determines the RGB triplet value to find; such that, the particles will update at each state and locate the designated target. Fig. 2(b) shows four frames of the performance associated with the particle filter point tracking algorithm. In this tracking problem, the desired target is red; therefore,

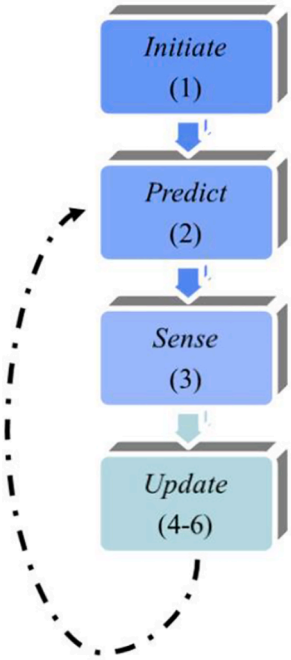

1- Initiate M number of particles: (Since the posterior distribution is unknown, the samples will be random, with time stamp i)

$$\Pi := \{\mathbf{X}_{i-1}^1, \mathbf{X}_{i-1}^2, \mathbf{X}_{i-1}^3, \ldots, \mathbf{X}_{i-1}^m\}$$

2- Predict the next state of all the particles in Π *based on the system model in Equation (10) and empty the* Π*:*

$$\overline{\Pi} := \{\mathbf{X}_{i-1}^1, \mathbf{X}_{i-1}^2, \mathbf{X}_{i-1}^3, \ldots, \mathbf{X}_{i-1}^m\}$$
$$\Pi := \{\}$$

3- Make a measurement of the predicted particle states:

$\mathbf{Y}_i$*: RGB values of the predicted pixels.*

4- Compute the likelihood of measurement for all the predicted particles in $\overline{\Pi}$*:*

$$\xi_m = P(\mathbf{Y}_i \mid \mathbf{X}_i^m)$$

5- Resample the new particles $\widehat{\mathbf{X}}_i^m$ *from* $\overline{\Pi}$ *(with replacement) while the probability of* $\mathbf{X}_i^m$ *being selected is proportional to* ξ_m*. Populate the* $\Pi := \{\}$ *with the new resampled particles:*

$$\widehat{\mathbf{X}}_i^m \rightarrow \Pi$$

6- The updated Π *are the new states. Make* $\overline{\Pi}$ *empty and go to 2 and repeat*

$$\overline{\Pi} := \{\}$$

Fig. 1. Description of the particle filter algorithm used for ODS extraction.

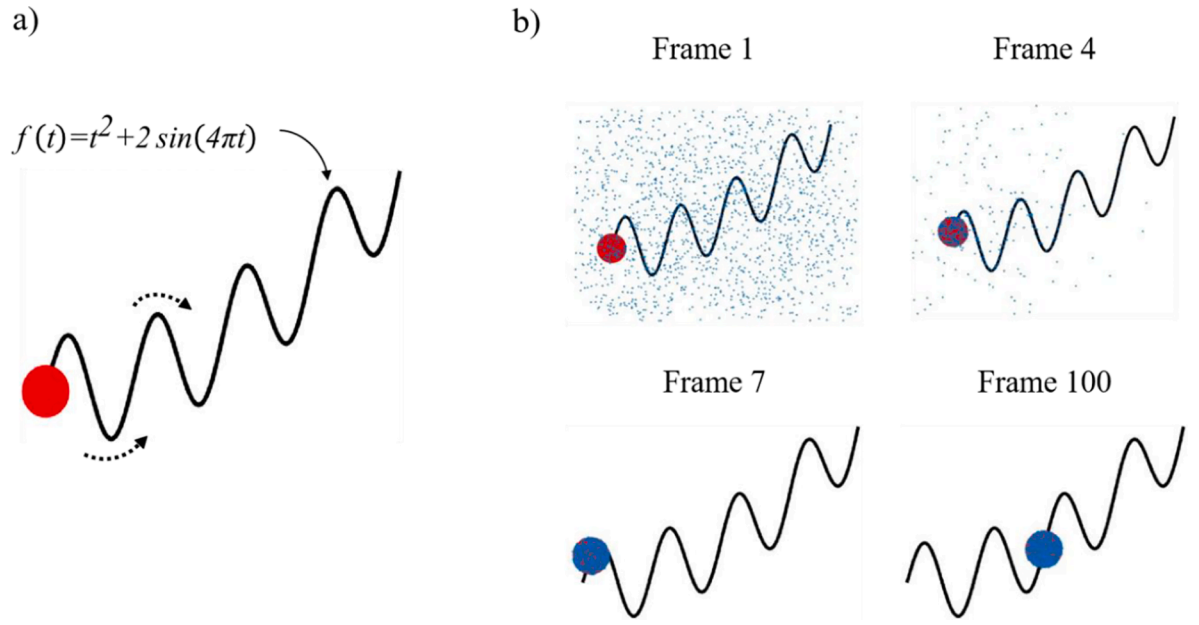

Fig. 2. (a) Trajectory of red of target, where$f(t) = t^2 + 2\sin(4\pi t)$. (b) Generated point cloud containing 10,000 particles tracking the distinct RGB target for time step: 1, 4, 7 and 100.

$\overrightarrow{RGB_t} = [255, 0, 0]$. At the first frame of the tracking, Frame 1, the particles are sampled under a random distribution. In Frame 4, the target appears in the analysis domain and the particles with a higher ξ value will be sampled more often. After a few frames of applying the particle filter tracker, all the particles with poor consistency with both the defined motion model and $\overrightarrow{RGB_t}$ will be removed. These particles will be replaced with ones that are highly correlated to the $\overrightarrow{RGB_t}$ and the motion model. Within the proposed framework for transforming the motion-magnified sequence of images into quantified ODS vectors, a particle filter will be used to eliminate the unreliable edge detection procedure.

2.4. Clustering

Using a particle filter is shown to be adequate for tracking a single target as shown Fig. 2. Averaging the location of all the particles in the field of view (FOV), will provide an estimation for the location of the target. With regards to structural dynamics, the objective is to track multiple targets to reconstruct a reliable and smooth mode shape or ODS vector. The multimodal estimator characteristic of the particle filter permits tracking multiple targets simultaneously. Therefore, the particles will be attracted to multiple points of interest in the same frame if there are multiple instances of pixels containing the desired $\overrightarrow{RGB_t}$. However, in this case, by averaging the location of all the particles, the result will be an arbitrary point with implies eventual failure of the tracking and mode extraction. To avoid this problem, all the particles should be clustered first, and then the averaging would take place among the particles that are grouped as a

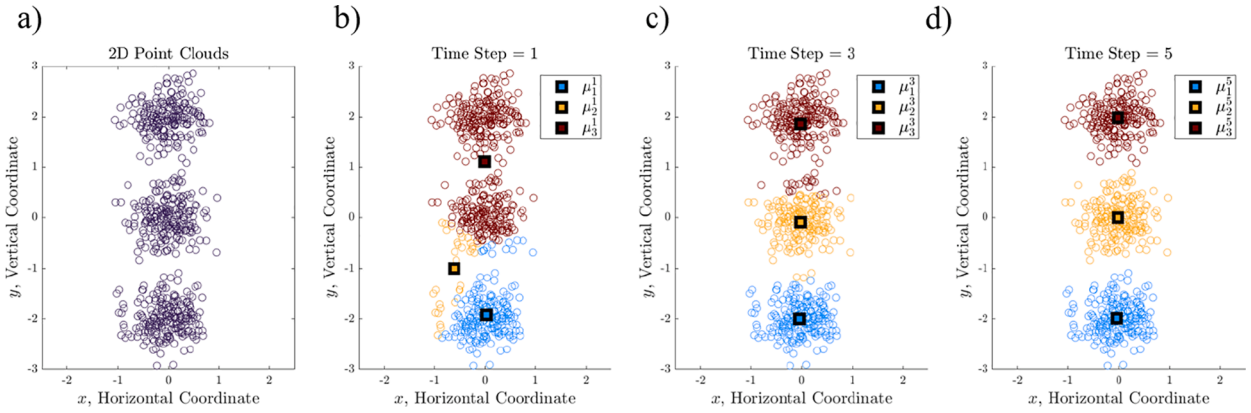

Fig. 3. a) Raw data points before clustering. b-d) Iterations: 1, 3 and 5 of the k-means clustering algorithm.

unique cluster. Clustering is categorized as an unsupervised learning problem that can extract structure from an unlabeled dataset [58]. Among several clustering methods available in the context of unsupervised learning methods, k-means clustering algorithm is utilized in this work [59]. The k-means algorithm involves the averaging stage during the clustering procedure. As a result, the cluster centers associated with the cluster labels will be available once the convergence criteria of the algorithm are satisfied. The details on k-means clustering method and the proof of convergence can be found in machine learning textbooks and references [60]. In this application, a set of 2D points are initiated by populating the set $\widehat{P}$ with the location of all the particles at time step i as $\widehat{P} = [p_1, p_2, p_3, \cdots, p_m]$. The objective is to cluster a set of points $\widehat{P} = [p_1, p_2, p_3, \cdots, p_m]$ in the 2D image. Each point represents the location of the particles in the particle filter algorithm. An intuitive algorithm for solving this optimization problem is outlined in [58].

This algorithm will always converge to the local optimal solution of the optimization problem. The convergence of the clustering algorithm will result in, μ_k^m, which describes coordinates for k number of point clouds and m number of states. Fig. 3 shows an example of the convergence in k-means algorithm, which will be to perform clustering with the particles that are attracted to multiple target locations. Assume that the data points in Fig. 3(a) are unlabeled particles that are attracted to three different targets in the scene. The objective is to divide the particles into three different groups to represent each of the three targets. Fig. 3(b) through Fig. 3(d) show the convergence and clustering procedure using the k-means algorithm. As displayed in Fig. 3(b), the cluster centers are initiated randomly. Convergence is ultimately achieved for the desired number of clusters as the assignment of particles begins due to sequential updating.

2.5. Outlier removal via total variation denoising

PMM is notorious for producing ringing effects, which ultimately can create gray-scale variation in images. This high-frequency ringing can cause inaccurate placement of particles and subsequent clusters. Total variation, as introduced by Rudin et al., has been implemented over a wide variety of image based analyses [61,62]. In addition, this image processing technique has been used to suppress phase-based motion magnification artifacts for frequency validation [63]. Equation (15) defines the iterative process using the divergence operator ∇ where K and $\widetilde{K}$ are the magnified smoothed images respectively.

$$\frac{\partial \widetilde{K}}{\partial t} = \nabla \bullet \left(\frac{\nabla \widetilde{K}}{\|\nabla \widetilde{K}\|} \right) + \beta \left(K - \widetilde{K} \right) \tag{15}$$

The non-trivial selection of the regularization parameter β provides a degree of smoothing. Its value can range from 0 to 1, where smoothing becomes more severe as it approaches its minimum allocation. The images are deemed smooth when the total variation becomes equivalent to the gradient magnitude. This process is achieved after a series of computations ,h, which can be set to a desirable amount. Fig. 4 displays the systematic procedure that is used to yield the processed images that can be inputted into the particle filter algorithm. The hand-speckled pattern that is seen in the foreground is highlighted using common image processing techniques such as

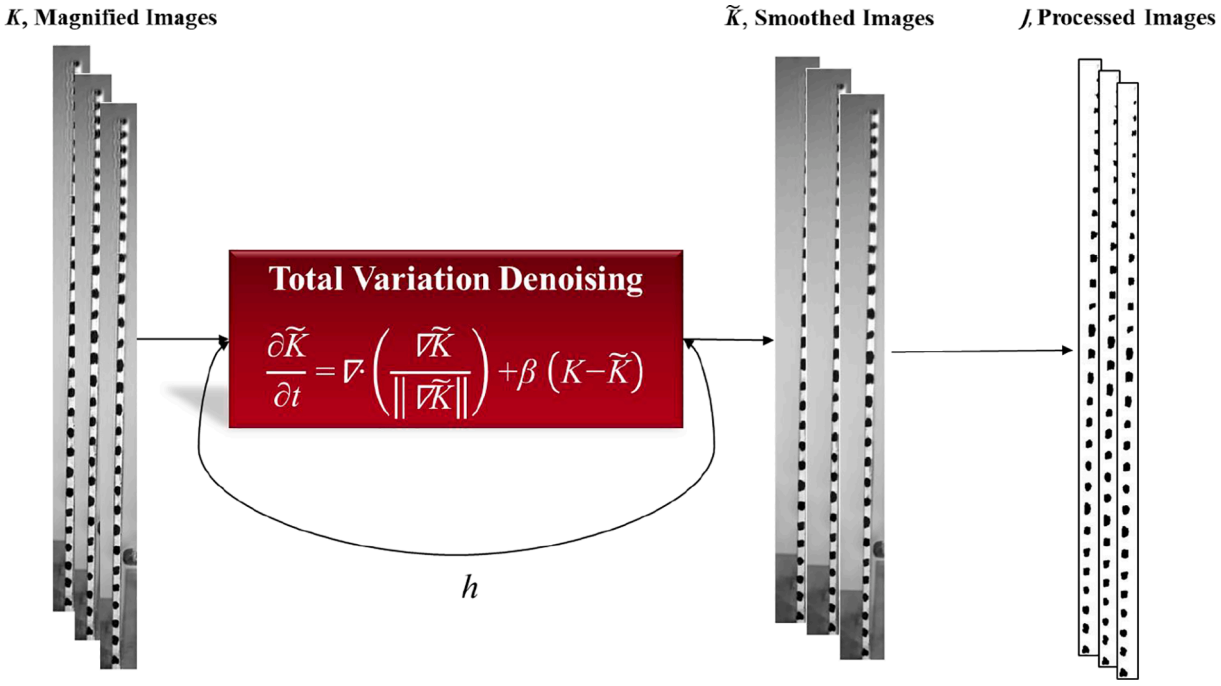

Fig. 4. Image denoising process for artifact and outlier removal. For each of the four magnified videos, $\beta = 0.5$ and $h = 100$.

erosion and adaptive thresholding. This ultimately produces a series of processed images,*J*. This approach will remove any background information that will contaminate the extraction of ODS vectors.

Following the smoothing and definition of each hand-speckled target, the processed frames are entered into the particle filtering algorithm for ODS extraction.

At this point, the theoretical background on the tools for structural dynamics identification via a hybrid-computer vision approach has been described. In the next section, these techniques will be merged to construct the framework to estimate ODS, and the overall picture of the methodology will be revisited.

3. Workflow and procedures

As aforementioned, the use of particle filtering and clustering algorithms will automate the extraction of ODS vectors for system dynamics identification and SHM applications. As discussed previously, the variations of the phase will be proportional to the actual motion of the vibrating structure. Therefore, the resonant frequencies of the structure can be obtained by analyzing the variations of the phase in the frequency domain. Having a reliable estimation of the resonant frequencies of the structure is crucial for the motion magnification process. This is due to the structuring of the band-pass filters where the center frequencies of the band-pass filters used for PMM will be selected based on the resonant frequencies from PME, as shown in Fig. 5.

Once the resonant frequencies of the structure are available, the motion magnification algorithm will be used to magnify the subtle vibrations of the structure in designated frequency bands. At this point of the analysis, the visual perception of the ODS is available which can provide qualitative knowledge regarding the structure's motion patterns. Visual perceptions are not considered sufficient for engineering purposes ranging from model updating to SHM decision making. To convert the visual perceptions into quantified ODS vectors in a reliable and semi-automated manner, the next stage concerns applying the particle filter point tracking on the motion-magnified videos. Applying phase-based motion magnification before the particle filter tracker is necessary because the PMM is more sensitive to small motions compared to the particle filter. By applying the PMM, the higher order modes of the structure can also be identified. Applying the particle filter algorithm on the raw video may only extract the lowest or lower order modes that dominate the dynamic motion. Due to the ghosting artifacts that appear at larger magnification factors, total variation denoising in used to smooth high frequency noise that appear in exaggerated video.

At this stage, all the particles will be attracted to the multiple targets on the hand-speckled structure. Therefore, the particles will be clustered using the k-means clustering method, which will separate the particles into individual clusters. Each cluster found will correspond to one of the targets. The location of targets can be estimated with the cluster centers, so that the quantified ODS vectors can be extracted automatically. Fig. 6 shows the overall structure of the proposed magnified video processing methodology for ODS extraction.

The main advantage to this approach is that the human supervision and intervention in the process of transforming the motion-magnified videos to the quantified ODS vectors will be decreased considerably.

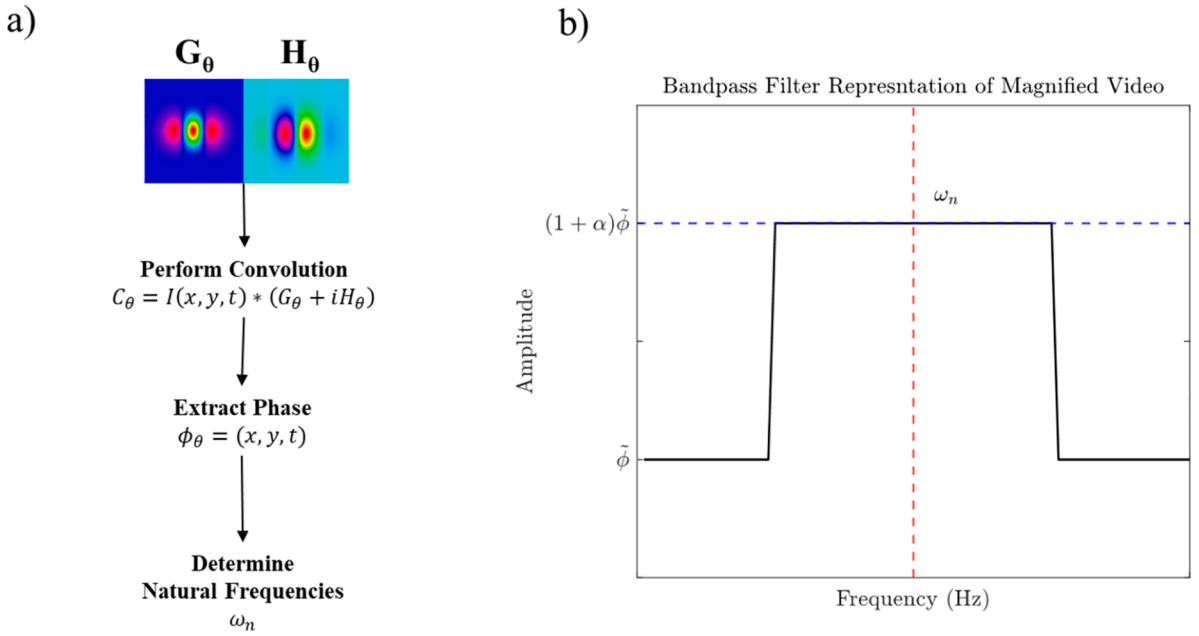

Fig. 5. a) Phase-based motion estimation (PME) algorithm methodology; b) Design of the band-pass filter used for PMM based on the resonant frequencies found from PME.

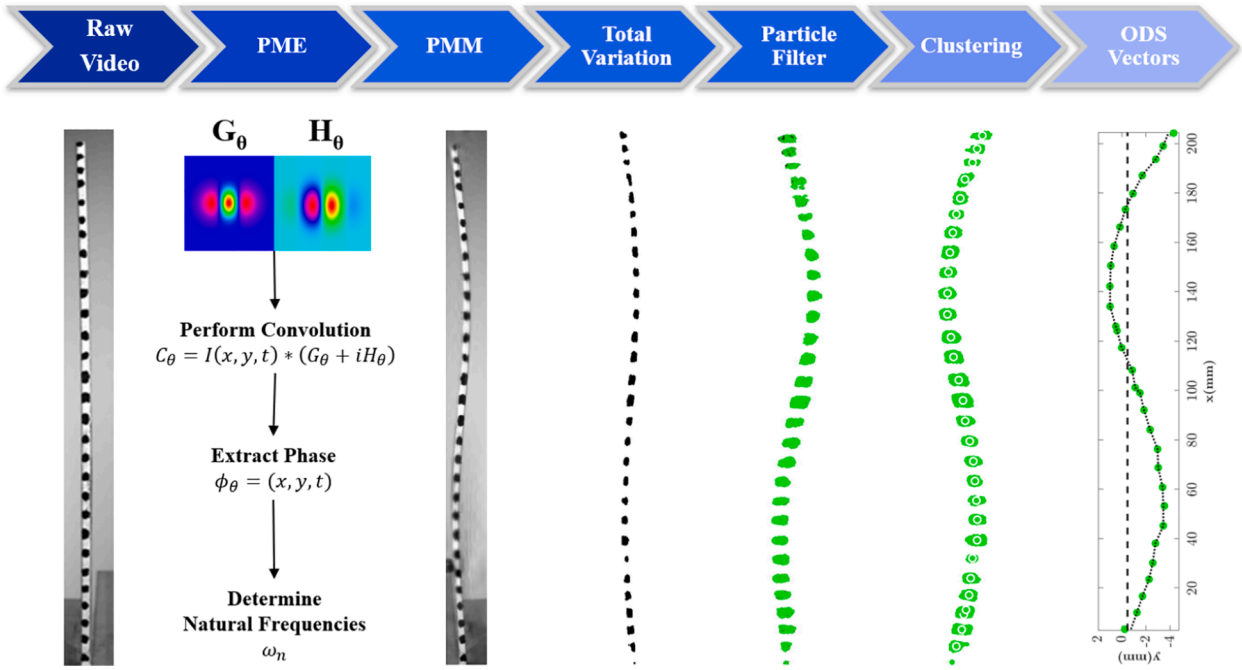

Fig. 6. The general workflow of the proposed method for extracting the quantified ODS vectors. In this figure, the capturing of a third bending ODS is depicted.

4. Experimental test setup and FEM

The performance of the proposed methodology is evaluated on a benchmark lab-scale cantilever beam. Fig. 7 shows the overview of the test setup, where the beam is clamped at the bottom of the test structure. The cantilever beam is excited with a modal impact hammer near the bottom of the beam to excite higher order dynamics. A Photron FASTCAM-CMOS high-speed camera records the video of the vibrating cantilever-beam at a rate of 2500 frames per second (fps). To enhance image quality, high contrast black dots are painted on the beam before testing, which will be used later as feature points for ODS vector extraction. Fig. 7(a-b) show the CMOS high-speed camera and the cantilever beam. Fig. 7(c) shows the field of view of the camera while capturing the sequence of images from the vibrating beam.

The reliability PME and PMM in structural dynamics identification have been evaluated several times in the literature [21,28,63-

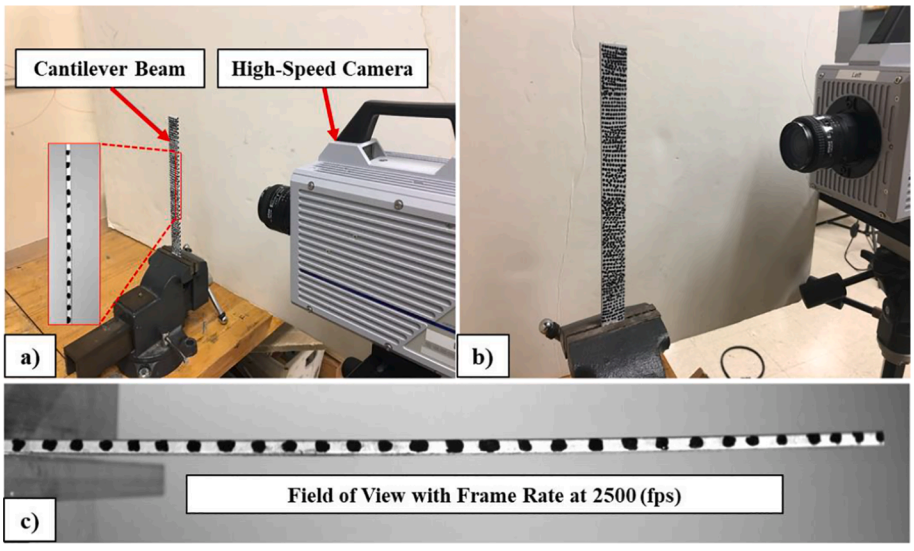

Fig. 7. (a-b) The CMOS high-speed camera and the cantilevered beam test structure, (c) field of view for the camera capturing the sequence of images of the vibrating beam.

65]. Nonetheless, for validation of this specific case study, a finite element model (FEM) of the test structure is established in ABAQUS/CAE. The material properties of the test article and FEM parameters are outlined in Table 1 below.

The lower part of the beam is subjected to a horizontal impact, and the boundary condition of the beam is considered fixed in all directions as shown in Fig. 8(a).

As an additional validation technique, the frequency response function (FRF) between two measurement points on the cantilever beam is obtained using an accelerometer. This will be used to validate the estimated natural frequencies obtained from PME and FEM. Fig. 8(b) shows the experiment layout used for FRF measurement.

5. Results and discussion

The results and discussion section is divided into two parts. The first part discusses the results of PME and the estimated resonant frequencies of the structure from the raw recorded video of the vibrating cantilever beam. The second part is mainly focused on transforming the motion-magnified videos (visual perceptions) to quantified ODS vectors.

5.1. Resonant frequencies

As mentioned earlier, the variations of the phase in the sequence of images are proportional to the actual subtle motions of the surface of the structure. Therefore, the phase variations and the actual motion must have the same frequency content. In other words, the location of the peaks in the frequency domain representation of the phase signal is equivalent to the resonant frequencies of the cantilever beam. It is worth mentioning that the variations of the phase are always measured with respect to the first frame of the video as the reference point in time. Fig. 9 shows the signal of phase variations in the frequency domain and the resonant frequencies of the cantilever beam can be easily identified by observing the dominant peaks.

As a final validation for the estimated resonant frequencies obtained from PME, Fig. 10 displays FRF between a measured impact and accelerometer response. Table 2 shows the comparison of extracted resonant frequencies using EMA, FEM and PME.

The estimated resonant frequencies of the beam that are obtained from three different sources are presented in Table 2. Due to the mass loading effect from the accelerometer, resonant frequencies from EMA will decrease slightly compared to the results gathered from PME and FEM. This ultimately could provide inaccuracies in measurement, which are typically not seen from optical or finite element approaches. Although correlation is seen between FEM and PME, it should be noted that discrepancies in resonant frequencies can be caused due to a coarsely defined mesh. Typically, a coarsely defined mesh will aid computation time; however, optimization and accuracy of FEM are beyond the scope of this work. Ultimately, the results shown in Table 2 indicate that the PME can provide consistent estimations of the resonant frequencies of the cantilever beam.

5.2. Operating deflection shapes

Center frequencies of the band-pass filters are selected as the resonant frequencies of the beam that were estimated using PME. The width of the passband of the filter is set to be $b = 1.5$ Hz for all four ODSs. The relative displacement will decrease for higher order modes; therefore, the magnification factor α increases for the higher order ODS. For example, the amplification factor for the first ODS is $\alpha = 10$, due to the first mode dominating the dynamic motion captured in video. On the contrary, the fourth ODS is not perceivable in the raw video so it will require a magnification factor of $\alpha = 100$.

Fig. 11 is the visual perception of all four ODS and provides an intuitive understanding of the qualitative data. The location nodes and antinodes for each ODS can be identified visually. Due to the amplification of subtle motion, ghosting artifacts tend where the motion has reached its local extrema. For engineering applications, deflection extrema of ODS should be quantified. Applying the next stages of the proposed methodology will lead to reliable and quantified ODS vectors.

The particle filter point tracking is applied to each of the four motion-magnified videos. The number of particles is selected using 25% of the total number of pixels present in the image. This number of particles provide efficient execution time and accuracy of the algorithm. In this case study, the images are 1600 by 256 indicating that there are 409,600 pixels. Therefore, 102,400 particles are used for tracking the hand-speckled targets. As Fig. 12 shows, the particles are attracted to the desired targets along the length of the cantilever beam. One of the advantages of the particle filter point tracking over traditional edge detection is that particle filters are less sensitive to background features. In consequence, the user can mount desired targets with unique features on the structure and track them throughout a sequence of frames. In addition, in most motion-magnified videos, distortions and artifacts occur very close to the

Table 1
List of FEM parameters used for ABAQUS/CAE simulation.

Property	Value
Density	7850 (kg/m3)
Young's Modulus	195 (GPa)
Poisson's Ratio	0.28
Geometric Dimensions of Cantilever Beam	205 mm × 25 mm × 3 mm
Element Size	1 (mm)
Number of Elements	780

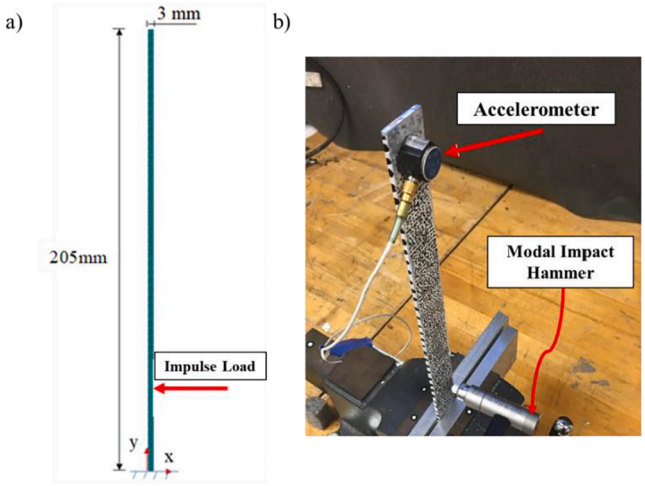

Fig. 8. (a) The geometry of the ABAQUS model of the beam, (b) The setup for measuring the FRF using the accelerometer and modal hammer.

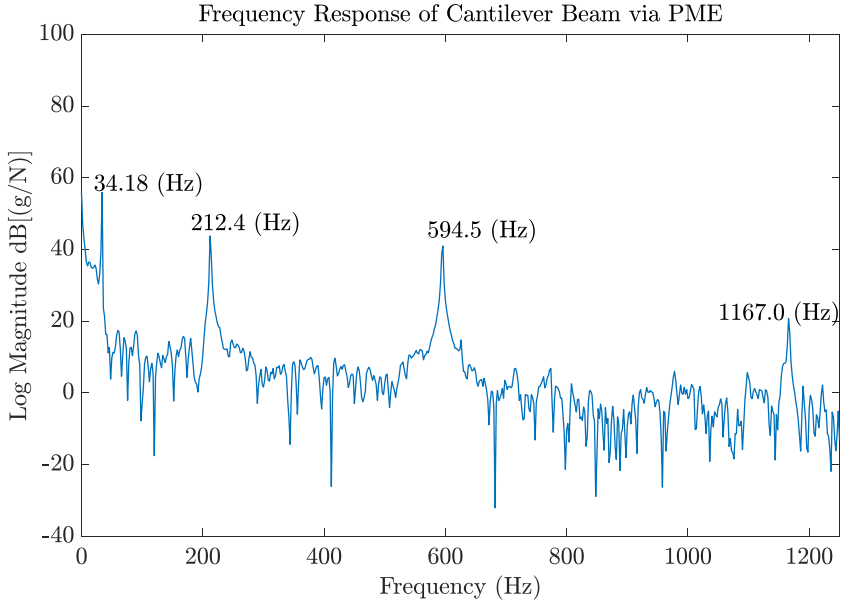

Fig. 9. Frequency response of the phase variation time-series extracted via PME. The peaks are located at the resonant frequency of the cantilever beam.

extrema of oscillatory motion. These artifacts are most likely detected with edge detection algorithms, which may lead to the false representation of the ODS vector.

$\overrightarrow{RGB_t}$ in Equation (14) as well as σ^2 are defined by the user. Defining $\overrightarrow{RGB_t}$ is straightforward for the hand-speckled targets because they contain a uniform pixel intensity. In The targets are black for each case; therefore, $\overrightarrow{RGB_t} = [15, 15, 15]$ and $\sigma^2 = 20$. The particle filter algorithm has an acceptable margin of robustness to the variations of these variables. It should be noted that some particles might get attracted to the locations on the background of the scene, if they have similar intensities to the desired targets. These outlier particles can be partially dealt with using several well-suited techniques to filter out the outliers such as total variation denoising, which will be discussed in the following section. The sensitivity of the particle filter to the background and other artifacts are considerably less than edge detection, because the edges are very low-level features of an image. Also, they tend to appear on the background more often compared to individual targets that are mounted on a structure.

All the particles are attached to the desired targets as the particle filter incrementally updates the likelihood function, but they are not assigned to a specific target. In other words, the particles presented in Fig. 12 are a 2D point cloud with no specific structure. This issue is resolved by applying a clustering algorithm on the 2D point cloud. The k-means clustering algorithm is applied, which partions the particles into individual groups. There are 29 targets on the beam; on account of this, 30 cluster centers were chosen for the k-

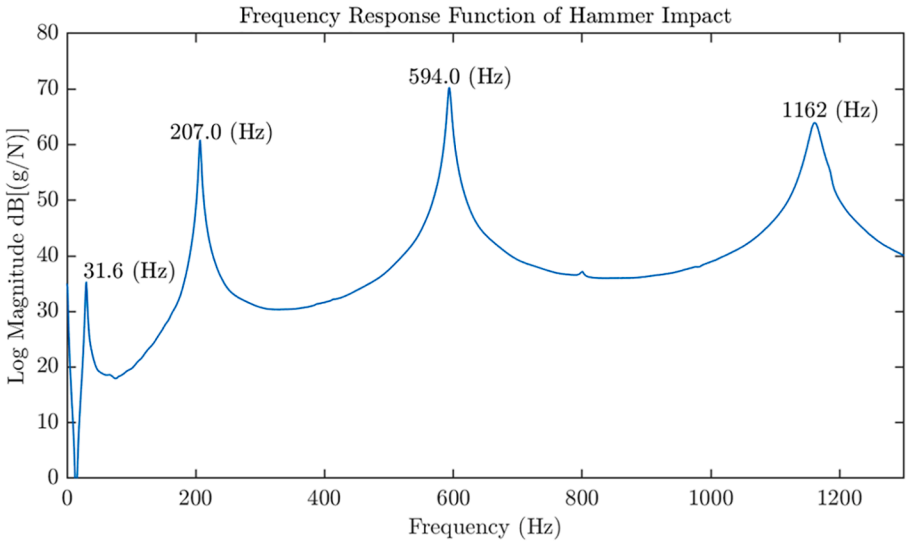

Fig. 10. FRF of the accelerometer with respect to the impact hammer force measurement.

Table 2
Comparison of resonant frequencies obtained from EMA, FEM and PME.

Mode Number	PME (Hz)	EMA (Hz)	FEM (Hz)	Frequency Difference, EMA vs. PME (%)	Frequency Difference, FEM vs. PME (%)
1	34.2	31.6	33.7	7.6	1.5
2	212.4	207.0	211.0	2.5	0.7
3	594.5	594.0	590.3	0.1	0.7
4	1167.0	1162.0	1155.0	0.4	1.0

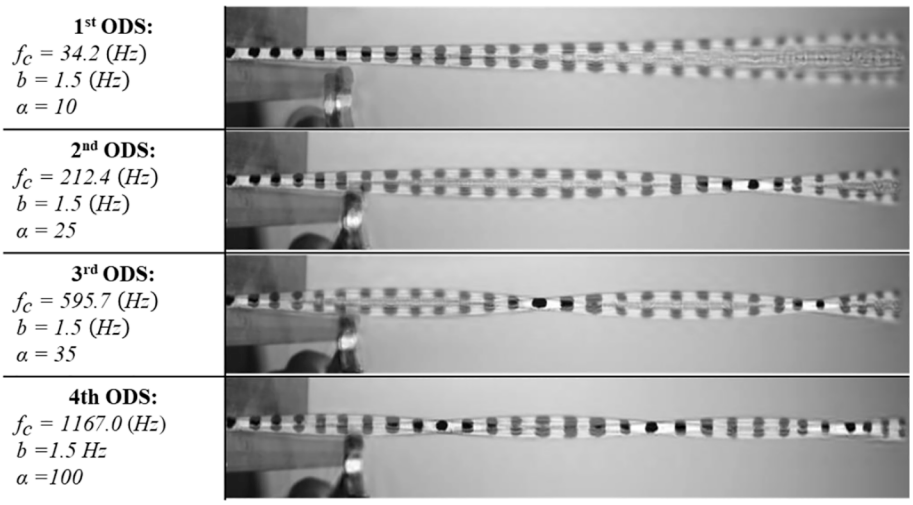

Fig. 11. ODS of the cantilever beam with corresponding parameters used for magnification.

means clustering algorithm. An additional number of clusters was chosen to ensure capturing of all targets captured in the scene. In general, the algorithm is relatively robust with regard to the number of selected cluster centers. However, selecting an abundance number of cluster centers may introduce unnecessary computations. The cluster centers of each 2D point cloud can be used to estimate the ODS of the structure. Fig. 13 shows the grouped particles with color-coding based on the order of ODS.

After clustering all 2D point clouds, the transformation of the motion-magnified videos to quantify ODS vectors is established. For a better visualization, Fig. 14 displays the cluster centers for each of the four ODS. As Fig. 14 shows, the quantified ODS vectors of the

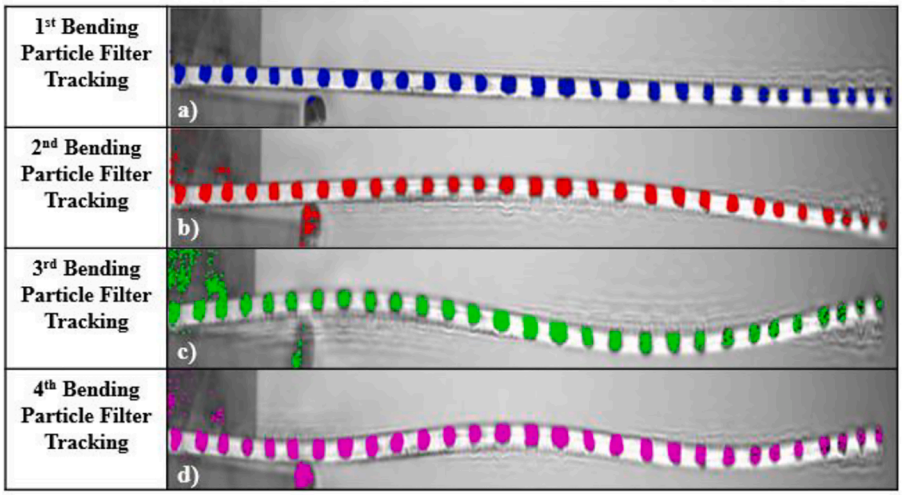

Fig. 12. Particle filter target tracking applied on motion-magnified videos for: (a) 1st Bending ODS, blue particles (b) 2nd Bending ODS, red particles (c) 3rd Bending ODS, green particles (d) 4th Bending ODS, pink particles.

cantilever beam are extracted in a semi-automated procedure.$\overrightarrow{RGB_t}, \sigma^2$ and the number of cluster centers are determined by the user, while the rest of ODS vector estimation is deployed automatically.

For a quantitative comparison, the Modal Assurance Criterion (MAC) values between the estimated ODS vectors and the FEM mode shapes are presented in Table 3 and Fig. 15. To evaluate MAC values, the data points in the finite element model were interpolated to obtain a set of data points to match with the location of the targets present in the captured video.

The MAC values on the main diagonal are relatively close to one, which indicates a high correlation between the shapes obtained from the proposed approach and FEM. Moreover, the off-diagonal terms in the MAC matrix are close to zero which implies orthogonality across different modes. MAC values are computed for the frame where the beam is at its maximum deflection shape. In theory, ODS vectors are unscaled mode shapes, and multiplying the ODS vector with a non-zero number will not affect the MAC value. Using the frame where the beam is at its maximum deflection can provide a better signal to noise ratio when comparing ODS.

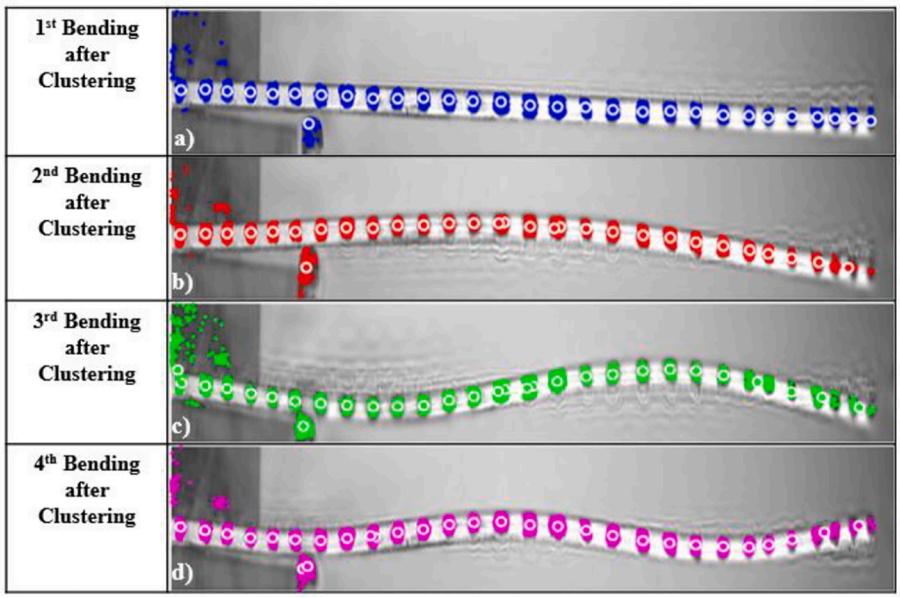

Fig. 13. Clustering the point clouds of particles for: (a) 1st Bending ODS, blue particles (b) 2nd Bending ODS, red particles (c) 3rd Bending ODS, green particles (d) 4th Bending ODS, pink particles.

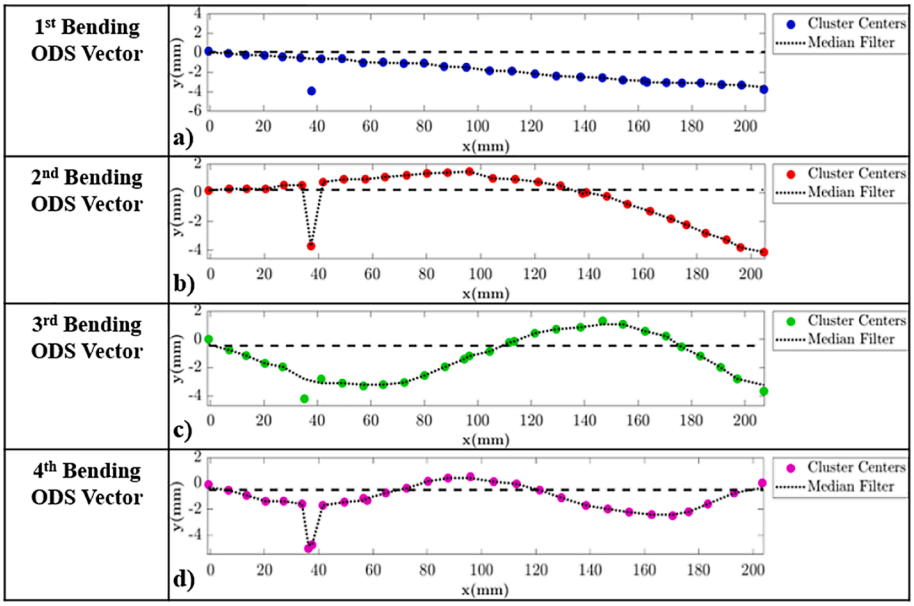

Fig. 14. Representation of the cluster centers as the estimated quantified vectors for: (a) 1st Bending ODS, blue particles (b) 2nd Bending ODS, red particles (c) 3rd Bending ODS, green particles (d) 4th Bending ODS, pink particles.

Table 3
Comparative analysis of extracted frequencies and MAC values at resonant frequencies.

Mode Number	FEM Frequency (Hz)	PME Frequency (Hz)	Frequency Difference (%)	MAC Value
1	33.69	34.18	1.45	0.972
2	211.0	212.4	0.66	0.957
3	590.3	594.5	0.71	0.953
4	1155.0	1167.0	1.04	0.920

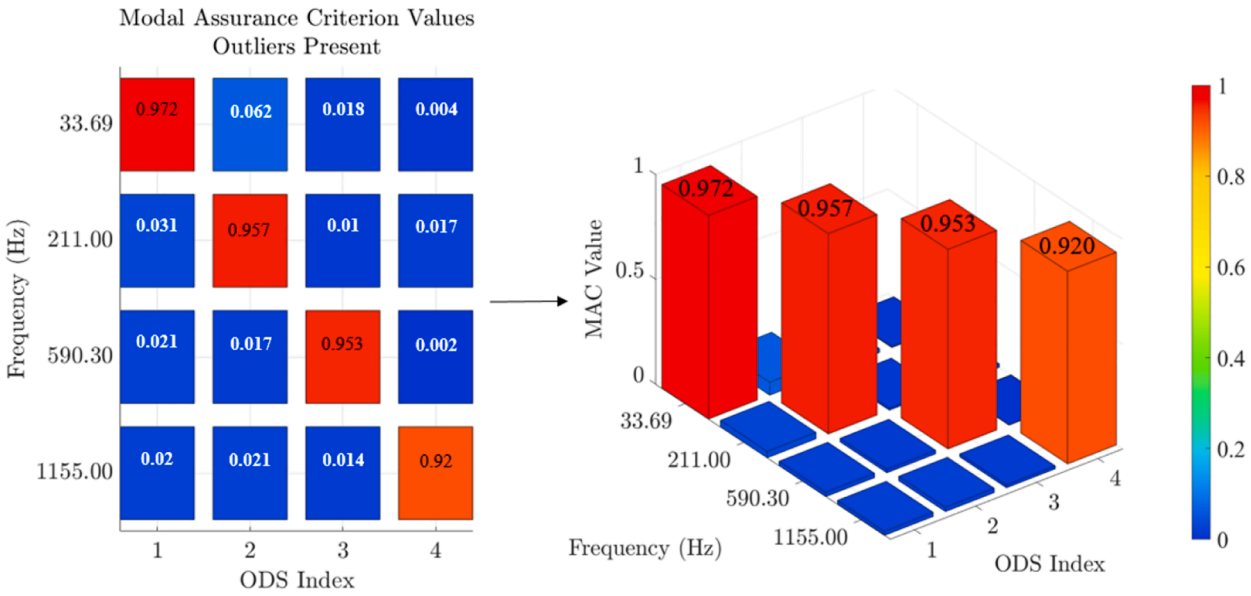

Fig. 15. Graphical representation of MAC values between PMM ODS vectors and modes shapes obtained from FEM.

5.3. Outlier reduction

The presence of outliers in the extracted ODS vectors drastically affect the accuracy of the result when compared to the finite element model. As aforementioned, total variation denoising can aid in smoothing ringing effects that appear following magnification of subtle motion. Following the procedure outlined in Fig. 4, Fig. 16 displays the clustered point clouds for each of the first four ODS vectors.

Outliers that were present in the original video were reduced due to the smoothing of motion-magnified artifacts in addition to suppression of background features. Fig. 17 depicts the estimated quantified ODS using the updated point cloud centers.

MAC values were computed once again using the updated ODS vectors in addition to the modal vectors gathered from the finite element model. This metric is re-computed to evaluate any potential improvements concerning ODS extraction. Table 4 and Fig. 18 list and display the updated MAC values post outlier removal.

The results obtained show improvement over the raw motion-magnified images; thus, providing a more accurate approximation of the corresponding operational deflection shapes. Fig. 19 presents a percent difference comparison between the two approaches used to quantify the first four ODS vectors.

It is seen that each MAC value is improved significantly following artifact and background suppression. Most significantly, the fourth extracted ODS vector is improved by approximately 3%, which shows the image processing is effective while handling high-frequency vibration.

6. Conclusions

This paper proposes a unified computer vision approach to magnified video data for structural dynamic identification. The motion-magnified videos are transformed into quantified ODS vectors with minimal human supervision and interference. PME is adapted to estimate resonant frequencies of the structure. The qualitative perception of the structural ODS are extracted by amplifying subtle vibration within specific frequency bands using PMM. The primary challenge this study aims to resolve is to find a semi-automated method to transfer motion-magnified videos into quantified ODS vectors. The particle filter is employed to perform point tracking on the motion-magnified videos, and afterward, the particles are clustered using the k-means clustering algorithm. It is shown in the paper that the cluster centers provide an accurate representation of a structure's ODS. The proposed methodology overcomes the drawbacks of conventional edge detection methods and requires significantly less human supervision. Furthermore, the hybrid non-contact approach's operational shapes MAC values for the first four modes range from 0.972 to 0.920 when compared to the finite element model. The proposed methodology requires elementary surface preparation, such as painting or mounting targets on the surface of the structure and is evaluated on a lab-scale cantilever beam. The method is further improved by implementing total variation denoising to smooth any potential artifacts that would affect quantification results. Due to the nature of high frequency dynamics, larger magnification factors are necessary to excite energy at higher order modes. Total variation can provide a robust outlier production for videos that require large amounts of magnification for structural dynamic identification. Specifically, the correlation of the fourth mode when compared to the finite element model is improved by 3%.

It should be noted that a significantly large magnification factor could ultimately degrade the particle filter's effectiveness in motion estimation due to the large amounts of spatial aliasing. Future studies will serve in investigating the particle filter's robust nature to handling larger motions seen in exaggerated videos. This includes an in-depth study into the sensitivity of the approach to factors such as: environmental noise that affect image data, background occlusions that appear in real-world applications, and observation noise related to particle filtering. In addition, investigations regarding the performance of the method on different types of structures with more complex geometry and sophisticated ODS vectors are necessary. Furthermore, the sensitivity of the methodology

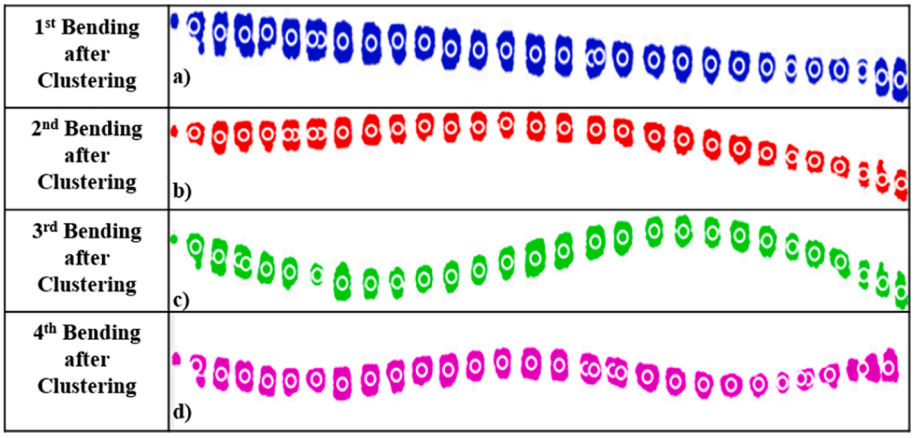

Fig. 16. Clustering the point clouds of particles used processed images: (a) 1st Bending ODS, blue particles (b) 2nd Bending ODS, red particles (c) 3rd Bending ODS, green particles (d) 4th Bending ODS, pink particles.

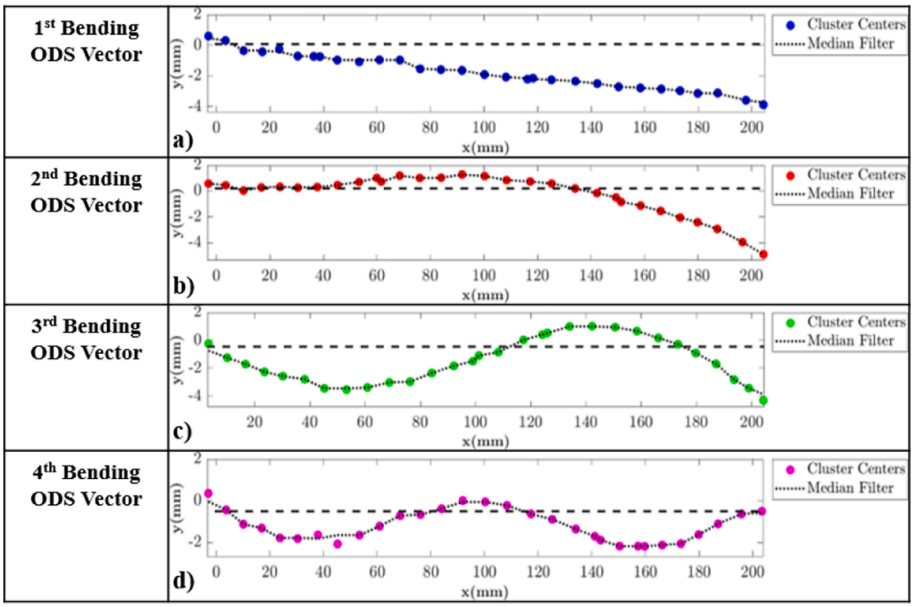

Fig. 17. Representation of the cluster centers as the estimated quantified vectors using processed images for: (a) 1st Bending ODS, blue particles (b) 2nd Bending ODS, red particles (c) 3rd Bending ODS, green particles (d) 4th Bending ODS, pink particles.

Table 4
MAC values between the ODS vectors obtained from PMM following outlier reduction.

Mode Number	FEM Frequency (Hz)	PME Frequency (Hz)	Frequency Difference (%)	MAC Value
1	33.7	34.2	1.45	0.987
2	211.0	212.4	0.66	0.980
3	590.3	594.5	0.71	0.971
4	1155	1167	1.04	0.952

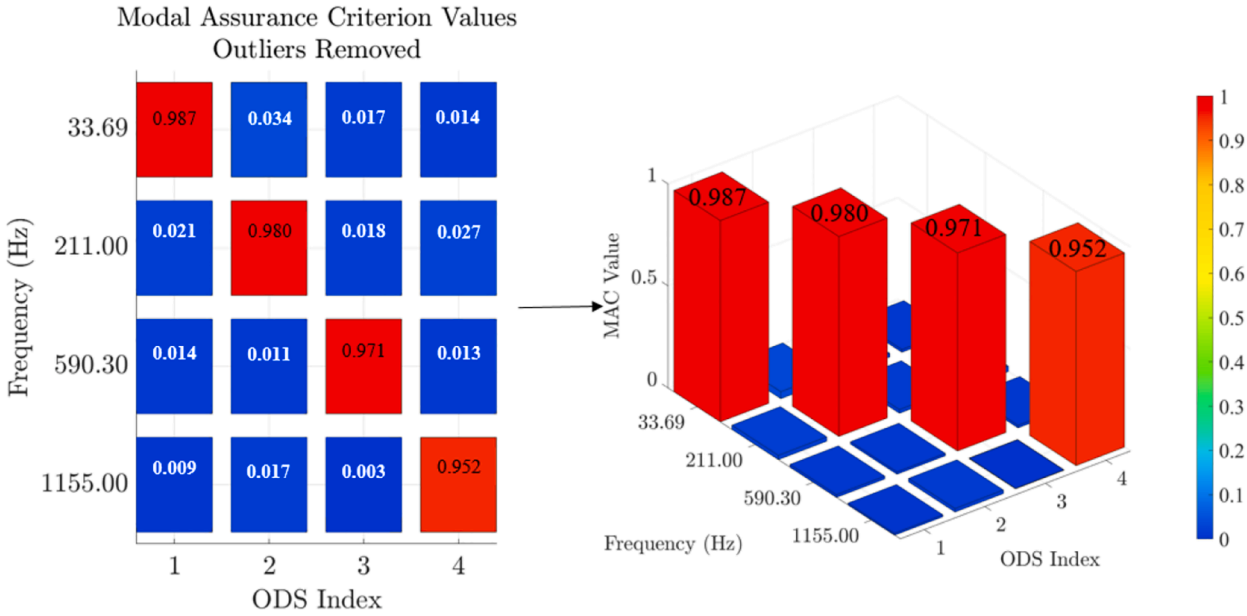

Fig. 18. Graphical representation of MAC values between smoothed PMM ODS vectors and modes shapes obtained from FEM.

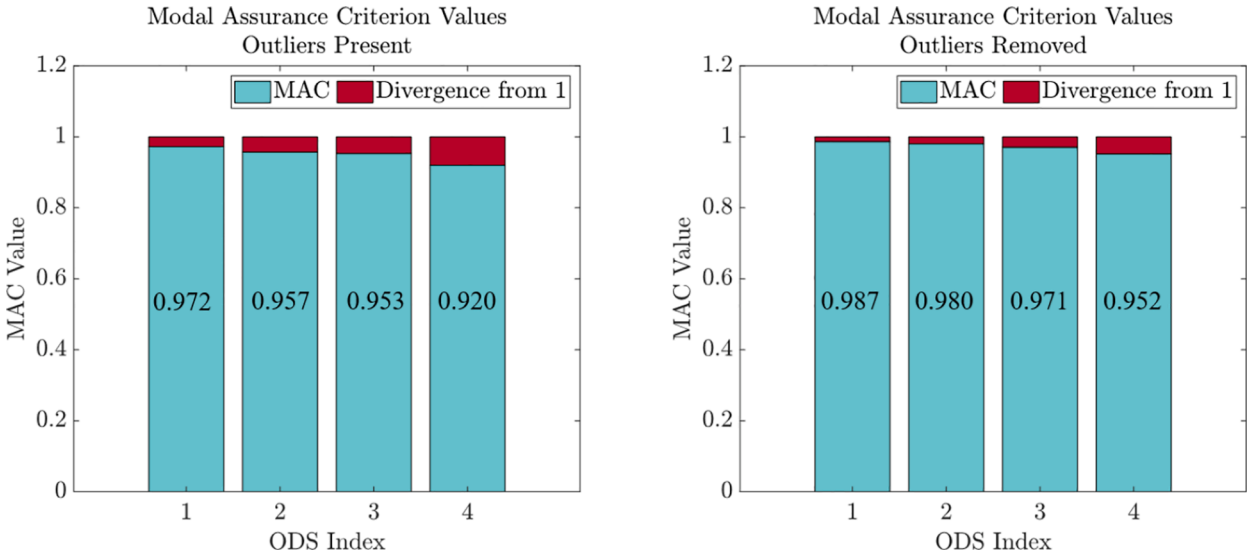

Fig. 19. Divergence comparison of MAC values pre and post outlier removal.

to the user-defined parameters, such as target RGB vector, the variance associated with the target RGB value, and the optimal number of cluster centers needs to be investigated further in future studies.

Declaration of Competing Interest

The authors declare that they have no known competing financial interests or personal relationships that could have appeared to influence the work reported in this paper.

Acknowledgements

This material is based upon work supported by the National Science Foundation under Grant No. 1762809. Any opinions, findings, and conclusions or recommendations expressed in this material are those of the authors and do not necessarily reflect the views of the National Science Foundation.

References

[1] E. Reynders, System identification methods for (operational) modal analysis: review and comparison, Arch. Comput. Methods Eng. 19 (1) (2012) 51–124.
[2] S.W. Doebling, C.R. Farrar, M.B. Prime, A summary review of vibration-based damage identification methods, Shock Vib. Digest 30 (2) (1998) 91–105.
[3] D.J. Ewins, Modal testing: theory and practice, Res. Stud. Press Letchworth (1984).
[4] E. Neu, F. Janser, A.A. Khatibi, C. Braun, A.C. Orifici, Operational Modal Analysis of a wing excited by transonic flow, Aerosp. Sci. Technol. 49 (2016) 73–79.
[5] D. Krichen, W. Abdallah, N. Boudriga, On the design of an embedded wireless sensor network for aircraft vibration monitoring using efficient game theoretic based MAC protocol, Ad Hoc Netw. 61 (2017) 1–15.
[6] A. Iliopoulos, R. Shirzadeh, W. Weijtjens, P. Guillaume, D.V. Hemelrijck, C. Devriendt, A modal decomposition and expansion approach for prediction of dynamic responses on a monopile offshore wind turbine using a limited number of vibration sensors, Mech. Syst. Sig. Process. 68–69 (2016) 84–104.
[7] O.D. Mohammed, M. Rantatalo, Dynamic response and time-frequency analysis for gear tooth crack detection, Mech. Syst. Sig. Process. 66–67 (2016) 612–624.
[8] X. Kong, J. Li, Vision-based fatigue crack detection of steel structures using video feature tracking, Comput.-Aided Civ. Infrastruct. Eng. (2018).
[9] X. Kong, J. Li, Image registration-based bolt loosening detection of steel joints, Sensors 18 (4) (2018) 1000.
[10] T.C. Huynh, J.H. Park, J.T. Kim, Structural identification of cable-stayed bridge under back-to-back typhoons by wireless vibration monitoring, Measurement 88 (2016) 385–401.
[11] C. Xiong, H. Lu, J. Zhu, Operational modal analysis of bridge structures with data from GNSS/accelerometer measurements, Sensors 17 (3) (2017) 436.
[12] G. Prakash, A. Sadhu, S. Narasimhan, J.M. Brehe, Initial service life data towards structural health monitoring of a concrete arch dam: structural health monitoring of a concrete arch dam, Struct. Control Health Monit. 25 (1) (2018) e2036.
[13] D. Feng, M.Q. Feng, Computer vision for SHM of civil infrastructure: from dynamic response measurement to damage detection–a review, Eng. Struct. 156 (2018) 105–117.
[14] D. Feng, M.Q. Feng, E. Ozer, Y. Fukuda, A vision-based sensor for noncontact structural displacement measurement, Sensors 15 (7) (2015) 16557–16575.
[15] C.T. do Cabo, N.A. Valente, Z. Mao, Motion magnification for optical-based structural health monitoring, in: P. Fromme, Z. Su (Eds.), Health Monitoring of Structural and Biological Systems XIV, SPIE, 2020, pp. 221–227, https://doi.org/10.1117/12.2559266.
[16] P. McDonald, G. Wiley, Modal analysis technology review, J. Acoust. Soc. Am. 85 (S1) (1989). S39-S39.
[17] J. Baqersad, C. Niezrecki, P. Avitabile, Extracting full-field dynamic strain on a wind turbine rotor subjected to arbitrary excitations using 3D point tracking and a modal expansion technique, J. Sound Vib. 352 (2015) 16–29.
[18] J. Baqersad, P. Poozesh, C. Niezrecki, P. Avitabile, Photogrammetry and optical methods in structural dynamics–a review, Mech. Syst. Sig. Process. 86 (2017) 17–34.
[19] P. Reu, Introduction to digital image correlation: best practices and applications, Exp. Tech. 36 (1) (2012) 3–4.
[20] I. Tomac, J. Slavič, Damping identification based on a high-speed camera, Mech. Syst. Signal Process. 166 (2022) 108485, https://doi.org/10.1016/j.ymssp.2021.108485.

[21] J.G. Chen, N. Wadhwa, Y.J. Cha, F. Durand, W.T. Freeman, O. Buyukozturk, Modal identification of simple structures with high-speed video using motion magnification, J. Sound Vib. 345 (2015) 58–71.
[22] J. Javh, J. Slavič, M. Boltežar, The subpixel resolution of optical-flow-based modal analysis, Mech. Syst. Sig. Process. 88 (2017) 89–99, https://doi.org/10.1016/j.ymssp.2016.11.009.
[23] Y.J. Cha, W. Choi, O. Büyüköztürk, Deep learning-based crack damage detection using convolutional neural networks, Comput.-Aided Civ. Infrastruct. Eng. 32 (5) (2017) 361–378.
[24] Y.J. Cha, W. Choi, G. Suh, S. Mahmoudkhani, O. Büyüköztürk, Autonomous structural visual inspection using region-based deep learning for detecting multiple damage types, Comput.-Aided Civ. Infrastruct. Eng. 33 (9) (2018) 731–747.
[25] Y.-J. Cha, K. You, W. Choi, Vision-based detection of loosened bolts using the Hough transform and support vector machines, Autom. Constr. 71 (2016) 181–188.
[26] J.-Y. Chou, C.-M. Chang, B.F. Spencer Jr, Out-of-plane modal property extraction based on multi-level image pyramid reconstruction using stereophotogrammetry, Mech. Syst. Signal Process. 169 (2022) 108786, https://doi.org/10.1016/j.ymssp.2021.108786.
[27] G. Liu, M.Z. Li, Z. Mao, Q.S. Yang, Structural motion estimation via Hilbert transform enhanced phase-based video processing, Mech. Syst. Signal Process. 166 (2022) 108418, https://doi.org/10.1016/j.ymssp.2021.108418.
[28] Y. Yang, C. Dorn, T. Mancini, Z. Talken, G. Kenyon, C. Farrar, D. Mascareñas, Blind identification of full-field vibration modes from video measurements with phase-based video motion magnification, Mech. Syst. Sig. Process. 85 (2017) 567–590.
[29] D. Gorjup, J. Slavič, A. Babnik, M. Boltežar, Still-camera multiview Spectral Optical Flow Imaging for 3D operating-deflection-shape identification, Mech. Syst. Signal Process. 52 (2021) 107456, https://doi.org/10.1016/j.ymssp.2020.107456.
[30] M.N. Helfrick, C. Niezrecki, P. Avitabile, T. Schmidt, 3D digital image correlation methods for full-field vibration measurement, Mech. Syst. Sig. Process. 25 (3) (2011) 917–927.
[31] J. Baqersad, P. Poozesh, C. Niezrecki, P. Avitabile, Photogrammetry and optical methods in structural dynamics – A review, Mech. Syst. Sig. Process. 86 (2017) 17–34.
[32] J. Tran, J. Sirohi, Implementation of Piezoelectric Shape Sensors Using Digital Image Correlation, in: Structural Health Monitoring Photogrammetry & DIC, Springer, 2019, pp. 133–136.
[33] E. Zappa, A. Matinmanesh, P. Mazzoleni, Evaluation and improvement of digital image correlation uncertainty in dynamic conditions, Opt. Lasers Eng. 59 (2014) 82–92.
[34] A. Sabato, N.A. Valente, C. Niezrecki, Development of a camera localization system for three-dimensional digital image correlation camera triangulation, IEEE Sens. J. 20 (19) (2020) 11518–11526, https://doi.org/10.1109/JSEN.2020.2997774.
[35] M. Angelosanti, S. Debetwar, E. Currá, A. Sabato, 3D-DIC analysis for BIM-oriented SHM of a lab-scale aluminium frame structure, J. Phys.: Conf. Series 2041 (1) (2021) 012009, https://doi.org/10.1088/1742-6596/2041/1/012009.
[36] N. Wadhwa, M. Rubinstein, F. Durand, W.T. Freeman, Phase-based video motion processing, ACM Trans. Graphics 32 (4) (2013) 1–10.
[37] N. Wadhwa, Revealing and Analyzing Imperceptible Deviations in Images and Videos. Massachusetts Institute of Technology, 2016.
[38] N. Wadhwa, M. Rubinstein, F. Durand, and W. T. Freeman, "Riesz pyramids for fast phase-based video magnification," ed: US Patent 9,338,331, 2016.
[39] N. Wadhwa, H.-Y. Wu, A. Davis, M. Rubinstein, E. Shih, G.J. Mysore, J.G. Chen, O. Buyukozturk, J.V. Guttag, W.T. Freeman, F. Durand, Eulerian video magnification and analysis, Commun. ACM 60 (1) (2016) 87–95.
[40] J.G. Chen, A. Davis, N. Wadhwa, F. Durand, W.T. Freeman, O. Büyüköztürk, Video camera-based vibration measurement for civil infrastructure applications, J. Infrastruct. Syst. 23 (3) (2017).
[41] N.A. Valente, C.T. do Cabo, Z. Mao, C. Niezrecki, Quantification of phase-based magnified motion using image enhancement and optical flow techniques, Measurement 189 (2022) 110508, https://doi.org/10.1016/j.measurement.2021.110508.
[42] Y. Yang, C. Dorn, T. Mancini, Z. Talken, S. Nagarajaiah, G. Kenyon, C. Farrar, D. Mascareñas, Blind identification of full-field vibration modes of output-only structures from uniformly-sampled, possibly temporally-aliased (sub-Nyquist), video measurements, J. Sound Vib. 390 (2017) 232–256.
[43] Y. Yang, C. Dorn, T. Mancini, Z. Talken, J. Theiler, G. Kenyon, C. Farrar, D. Mascareñas, Reference-free detection of minute, non-visible, damage using full-field, high-resolution mode shapes output-only identified from digital videos of structures, Struct. Health Monit. (2018), https://doi.org/10.1177/1475921717704385, p. 1475921717704385.
[44] A. Sarrafi, Z. Mao, C. Niezrecki, P. Poozesh, Vibration-based damage detection in wind turbine blades using Phase-based Motion Estimation and motion magnification, J. Sound Vib. 421 (2018) 300–318, https://doi.org/10.1016/j.jsv.2018.01.050.
[45] S. Bhowmick, S. Nagarajaiah, Z. Lai, Measurement of full-field displacement time history of a vibrating continuous edge from video, Mech. Syst. Signal Process. 144 (2020), https://doi.org/10.1016/j.ymssp.2020.106847.
[46] S. Bhowmick, S. Nagarajaiah, Spatiotemporal compressive sensing of full-field Lagrangian continuous displacement response from optical flow of edge: identification of full-field dynamic modes, Mech. Syst. Signal Process. 164 (2022), https://doi.org/10.1016/j.ymssp.2021.108232.
[47] D.J. Fleet, A.D. Jepson, Computation of component image velocity from local phase information, Int. J. Comput. Vision 5 (1) (1990) 77–104.
[48] I. Fogel, D. Sagi, Gabor filters as texture discriminator, Biol. Cybern. 61 (2) (1989) 103–113.
[49] W.T. Freeman, E.H. Adelson, The design and use of steerable filters, IEEE Trans. Pattern Anal. Mach. Intell. 13 (9) (1991) 891–906.
[50] J.G. Chen, N. Wadhwa, Y.-J. Cha, F. Durand, W.T. Freeman, O. Buyukozturk, Structural modal identification through high speed camera video: Motion magnification, in: Topics in Modal Analysis I, Springer, 2014, pp. 191–197.
[51] S. M. Kay, "Fundamentals of statistical signal processing, volume I: estimation theory," 1993.
[52] Y.-J. Cha, J. Chen, O. Büyüköztürk, Output-only computer vision based damage detection using phase-based optical flow and unscented Kalman filters, Eng. Struct. 132 (2017) 300–313.
[53] M.D. Breitenstein, F. Reichlin, B. Leibe, E. Koller-Meier, L. Van Gool, Robust tracking-by-detection using a detector confidence particle filter, in: Computer Vision, 2009 IEEE 12th International Conference on, IEEE, 2009, pp. 1515–1522.
[54] K. Okuma, A. Taleghani, N. De Freitas, J.J. Little, D.G. Lowe, A boosted particle filter: Multitarget detection and tracking, in: European conference on computer vision, Springer, 2004, pp. 28–39.
[55] C. Yang, R. Duraiswami, L. Davis, Fast multiple object tracking via a hierarchical particle filter, in: Computer Vision, 2005. ICCV 2005. Tenth IEEE International Conference on, IEEE, 2005, pp. 212–219.
[56] M. Marron, et al., Comparing a Kalman Filter and a Particle Filter in a Multiple Objects Tracking Application, in: 2007 IEEE International Symposium on Intelligent Signal Processing, 2007, pp. 1–6, https://doi.org/10.1109/WISP.2007.4447520.
[57] S. Thrun, W. Burgard, D. Fox, Probabilistic robotics, MIT Press (2005).
[58] A.K. Jain, Data clustering: 50 years beyond K-means, Pattern Recogn. Lett. 31 (8) (2010) 651–666.
[59] J.A. Hartigan, M.A. Wong, Algorithm AS 136: A k-means clustering algorithm, J. R. Statist. Soc. Series C (Applied Statistics) 28 (1) (1979) 100–108.
[60] L. Bottou and Y. Bengio, "Convergence properties of the k-means algorithms," in: Advances in neural information processing systems, 1995, pp. 585-592.
[61] L.I. Rudin, S. Osher, E. Fatemi, Nonlinear total variation based noise removal algorithms, Physica D 60 (1) (1992) 259–268, https://doi.org/10.1016/0167-2789(92)90242-F.
[62] A. Chambolle, V. Caselles, M. Novaga, D. Cremers, and T. Pock, "An introduction to Total Variation for Image Analysis," vol. 9, 2010, doi: 10.1515/9783110226157.263.

[63] N.A. Valente, Z. Mao, M. Southwick, C. Niezrecki, Implementation of Total Variation Applied to Motion Magnification for Structural Dynamic Identification, in: D. Di Maio, J. Baqersad (Eds.), Rotating Machinery, Optical Methods & Scanning LDV Methods, Springer International Publishing, 2020, pp. 139–144, https://doi.org/10.1007/978-3-030-47721-9_17.
[64] A. Sarrafi, P. Poozesh, C. Niezrecki, and Z. Mao, "Mode extraction on wind turbine blades via phase-based video motion estimation," in: SPIE Smart Structures and Materials+ Nondestructive Evaluation and Health Monitoring, 2017: International Society for Optics and Photonics, pp. 101710E-101710E-12.
[65] A. Sarrafi, Z. Mao, Wind turbine blade damage detection via 3-dimensional phase-based motion estimation, Struct. Health Monit. 2017 (2017).